Title	Multiband Dual-Mode Doherty Power Amplifier Employing Phase Periodic Matching Network and Reciprocal Gate Bias for 5G Applications
Authors(s)	Pang, Jingzhou, Dai, Zhijiang, Li, Yue, Li, Meng, Zhu, Anding
Publication date	2020-06
Publication information	Pang, Jingzhou, Zhijiang Dai, Yue Li, Meng Li, and Anding Zhu. "Multiband Dual-Mode Doherty Power Amplifier Employing Phase Periodic Matching Network and Reciprocal Gate Bias for 5G Applications." IEEE, June 2020. https://doi.org/10.1109/tmtt.2020.2971481.
Publisher	IEEE
Item record/more information	http://hdl.handle.net/10197/11747
Publisher's statement	© 2020 IEEE. Personal use of this material is permitted. Permission from IEEE must be obtained for all other uses, in any current or future media, including reprinting/republishing this material for advertising or promotional purposes, creating new collective works, for resale or redistribution to servers or lists, or reuse of any copyrighted component of this work in other works.
Publisher's version (DOI)	10.1109/tmtt.2020.2971481

Multi-Band Dual-Mode Doherty Power Amplifier Employing Phase Periodic Matching Network and Reciprocal Gate Bias for 5G Applications

Jingzhou Pang, *Member, IEEE,* Zhijiang Dai, *Member, IEEE,* Yue Li, *Student Member, IEEE,* Meng Li, *Student Member, IEEE,* and Anding Zhu, *Senior Member, IEEE*

***Abstract*—This paper presents a novel method to design the multi-band Doherty power amplifier (DPA). It is illustrated that phase periodic matching networks (PPMNs) can be used as multi-band impedance inverters, off-set elements and phase compensators to realize multi-band DPAs. Moreover, the number of Doherty operation bands can be further increased by employing the reciprocal gate biases. A 6-band dual-mode DPA with 1.8-2.2/3.9-4.3 GHz operation bands in Mode I and 1.52-1.72/2.38-2.53/3.67-3.82/4.53-4.68 GHz operation bands in Mode II using commercial GaN transistors is designed and implemented to validate the proposed method. The fabricated DPA achieves 8.7-13.5 dB gain and 39.6-41.5 dBm peak output power at all the designed bands. Drain efficiency of 49.2%-54.5% and 42.2%-56.7% is measured at 6 dB output back-off in Mode I and Mode II, respectively. When stimulated by a 5-carrier 100 MHz OFDM signal with 7.7 dB peak to average power ratio (PAPR), adjacent channel power ratio (ACPR) of better than -48.9 dBc can be obtained by the proposed DPA after digital predistortion with 35.5%-50.1% average drain efficiency at 1.65/1.95/2.45/3.75/4.1/4.6 GHz, respectively.**

***Index Terms*—Doherty power amplifier, dual-mode, GaN, high efficiency, multi-band, wideband, 5G**

I. INTRODUCTION

THE rapid development of modern wireless communication systems has been accompanied by a burst of new standards and frequency bands, which creates strong demand for multi-mode/multi-band wireless transceivers. In the forthcoming next generation wireless communication system, i.e., 5G, this demand becomes even intenser since not only the existing 4G bands must be covered but also many new frequency bands, e.g., Band N77 from 3.3 GHz to 4.2 GHz and Band N79 from 4.4 GHz to 5.0 GHz, are added [1], [2]. Moreover, in some new applications, such as unmanned aerial vehicles (UAV) mounted moving base-stations, it is more important to support multi-band/multi-standards functions, because the operation bands of these base-stations are required to be reconfigurable based on the specific locations [3].

As one of the most power consuming elements in wireless transmitters, power amplifier (PA) faces significant challenges in multi-band operation. To accommodate high peak to average power ratio (PAPR) signals and maintain high average power efficiency, Doherty power amplifier (DPA) has become one of the most widely used PAs in wireless base stations due to its low complexity and high reliability [4]–[20]. In recent years, many efforts have been made to expand the frequency band coverage of DPAs. By introducing techniques such as continuous mode impedance [13]–[15], post-matching architecture [16]–[19], integrated compensating reactance [20], [21] and complex combing loads [22]–[24], bandwidth of DPAs has been greatly extended. However, when the required operation bands are separated by more than one octave, it is still difficult to cover them with Doherty operation [25], [26]. Possible solutions are to employ dual/multi-band or reconfigurable structures which could not cover the whole frequency band.

By introducing techniques such as frequency-dependent design [5], [7], direct-matching transformer [6] and multi-band coupled networks [8], dual/multi band Doherty operation can be successfully achieved. Besides, multi-band Doherty operation can be also achieved by employing electronically tunable load modulation networks [10], [11]. Despite the Doherty function can be implemented over a wide frequency band, the reported dual/multi band [4]–[8] or reconfigurable [10], [11] DPAs suffer from narrow band feature in each operation band, affecting their applications in wideband scenarios. Particularly, in [12], the periodicity of transmission lines is used to realize multi-band DPAs. Although tri-band and quad-band DPAs are realized using multi-section transmission line structure, the operating frequency they achieved cannot theoretically be continuously adjusted. Moreover, the bandwidth achieved in [12] is also very narrow just as the other reported multi-band DPAs. In 5G, these conventional design methods are difficult to apply because the signal bandwidth will continue increase, e.g., the signal bandwidth in sub-6 GHz will be up to 200 MHz [1], [2]. Therefore, it is very attractive to explore new bandwidth extension techniques for DPAs, that can combine the conventional wideband, multi-band and reconfigurable design methods.

In this paper, a novel method for designing multi-band DPAs is proposed. It is illustrated that broadband matching networks with phase periodicity can be used to design the impedance inverters, off-set elements and phase compensators in DPAs, thus multi-band Doherty operation can be achieved

---

This work was supported in part by the Science Foundation Ireland under Grant Numbers 13/RC/2077, 17/NSFC/4850 and 16/IA/4449. This research was also funded in part by funding from the European Union's Horizon 2020 Research and Innovation Program under the Marie Sklodowska-Curie grant agreement number 713567. (*Corresponding author: Jingzhou Pang*)

J. Pang, Y. Li, M. Li, and A. Zhu are with the School of Electrical and Electronic Engineering, University College Dublin, Dublin D04 E4X0, Ireland. (e-mail: jingzhou.pang@ucd.ie; yue.li1@ucdconnect.ie; meng.li@ucdconnect.ie; anding.zhu@ucd.ie)

Z. Dai is with the School of Microelectronics and Communication Engineering, Chongqing University, 400044 Chongqing, China. (e-mail: daizj_ok@126.com)

due to the phase periodicity. It is also presented that, by transferring the functional elements in wideband DPAs to the phase periodic matching networks, multi-band DPAs with wide bandwidth in each band can be realized. On the basis of this, reciprocal gate biases are then introduced to further increase the number of operation bands by employing the dual-mode operation. A circuit topology employing lumped and distributed hybrid parameters and the corresponding parameter optimization method are proposed to realize the required phase periodic matching networks with flexible target bands. Compared with other reported multi-band DPAs, the proposed architecture provides wider bandwidth in each operation band. Furthermore, the proposed DPA can achieve operation bands distributed over multiple octaves which are very difficult for broadband DPAs to achieve. A multi-band DPA is designed and fabricated using the proposed architecture with 6 operation bands.

The rest of the paper is organized as follows. First, the theory of the proposed multi-band DPA is demonstrated in section II. The characteristic of employing the phase periodic matching networks in multi-band DPAs is discussed along with the analysis of the reciprocal gate bias configuration. In section III, the circuits architecture and design method to realize the related phase periodic matching networks are developed. Based on the theory and PPMN design method, the design strategy of realizing the proposed DPA with commercial GaN devices in section IV. Finally, measurement results of the fabricated DPA is presented in section V to validate the effectiveness of the proposed architecture along with a conclusion presented in section V.

II. PROPOSED MULTI-BAND DPA

Doherty power amplifier improves back-off efficiency by combining two amplifiers, a carrier amplifier biased at class-AB and a peaking amplifier biased at class-C, via load modulation. In conventional DPAs, a quarter wavelength transmission line (TL) is usually employed in the carrier branch as the impedance inverter to achieve proper load modulation, as shown in Fig. 1. Normally, the Doherty operation can be achieved at a operation frequency f_c where the electrical length of the employed TL is $90°$. In fact, because the TL is inherently a frequency periodic structure, namely, the phase shift of the signal periodically changes with the operation frequency when passing through the TL, this leads that the back-off carrier matching impedance periodically repeats along multiple frequencies, as illustrated in Fig. 2. The impedance value shown in Fig. 2 is normalized to the characteristic impedance of the employed TL inverter. Generally, if the equal-phase combining is established and the impedance condition at saturation for the Doherty operation is satisfied, the bandwidth of the DPA is mainly determined by the back-off impedance. In this case, if the phase periodicity of the impedance inverter is utilized, the DPA can thus be operated at multiple bands. From Fig. 2, we can see that Doherty operation can be achieved when the operation frequency $f = f_c, 3f_c, 5f_c, ...$, where f_c is the center frequency of the lowest band that the DPA is designed for.

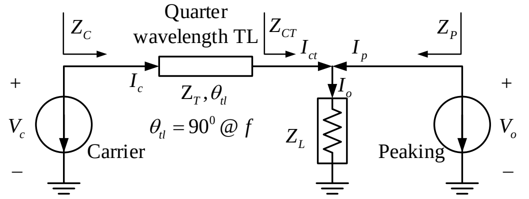

Fig. 1. The block diagram of the symmetrical DPA using only one TL as the impedance inverter.

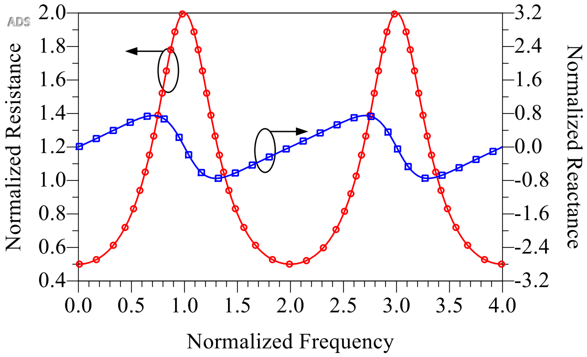

Fig. 2. Simulated carrier resistance and reactance at back-off region of the original DPA.

A multi-band DPA employing this phase periodicity characteristic has been introduced in [12], however, the frequency spacing of the operation bands for this kind of DPA has a fixed relationship and cannot be arbitrarily configured. Besides, each operation band of the designed DPA in [12] is also narrow, which is the same as that of many other reported multi-band DPAs. To solve the fixed frequency problem and to extend bandwidth, a new multi-band DPA is introduced in this work.

A. Multi-band DPA Using Phase Periodic Matching Networks

To solve the fixed frequency problem of the above mentioned DPA, a new network is introduced here to replace the quarter wavelength TL as the impedance inverter as shown in Fig. 3. The load of the DPA Z_L is set to $R_{opt}/2$ in this configuration, where R_{opt} is the optimal impedance of the carrier and peaking current generators (CGs). The introduced impedance inverter is a two port network and assume it is marched to Z_T at each port in a desired frequency band. The ABCD matrix of this network will have the similar expression as that of TLs with characteristic impedance of Z_T in this band, which can be expressed as,

$$\begin{bmatrix} A_{pp} & B_{pp} \\ C_{pp} & D_{pp} \end{bmatrix} = \begin{bmatrix} \cos\theta_{pp} & jZ_T\sin\theta_{pp} \\ j(\sin\theta_{pp})/Z_T & \cos\theta_{pp} \end{bmatrix} \quad (1)$$

where Z_T can be set as R_{opt}. θ_{pp} is the phase shift of the network and it can be defined as,

$$\theta_{pp} = -\frac{\pi}{2} \cdot (1 - \alpha) - \alpha \cdot \frac{\pi}{2} \cdot f_0 \quad (2)$$

where α is the slope of the phase shift and f_0 is the normalized frequency, $f_0 = f/f_c$ where f_c is still the center frequency of the lowest band when $\theta_{pp} = -\pi/2$.

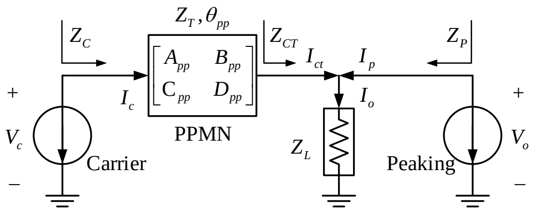

Fig. 3. The block diagram of the symmetrical DPA using using PPMN as impedance inverter.

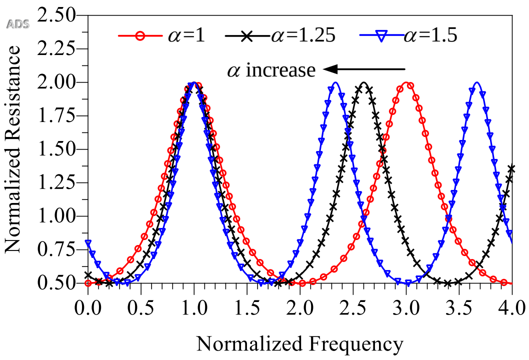

Fig. 4. Simulated carrier resistance at back-off region of the DPA using PPMN as impedance inverter for different values of α.

Based on the analysis introduced in [27] and [28], the carrier back-off impedance can be easily calculated as,

$$Z_{C,bo} = R_{opt} \frac{1 + j2\tan\theta_{pp}}{2 + j\tan\theta_{pp}}. \tag{3}$$

Equation (3) indicates that the bandwidth of DPAs using the proposed impedance inverter has the similar phase periodicity to the DPA using a quarter wavelength transmission line. We refer this kind of networks as the phase periodic matching networks (PPMN) in this article.

The difference from that using TL impedance inverter is that the frequency spacing between the bands can be arbitrarily configured. Fig. 4 presents the normalized carrier resistance at back-off region of the DPA using PPMN as impedance inverter for different values of α. It can be seen that, the operation frequency of this DPA will change as α changes. Therefore, a multi-band DPA can be designed with different band locations using a selected α. The detailed design procedure of the required PPMN will be discussed in Section III.

The above mentioned structure shown in Fig. 3 still has relatively narrow bandwidth in each target band, limiting its application in 5G systems where wide signal bandwidths are usually required. Therefore, it is important to design multi-band DPAs with wider bandwidth in each band. One of the effective ways to extend the bandwidth of DPA is to introduce a half wavelength TL in the peaking branch as an off-set line [29]. In this work, we generalize this bandwidth extension idea by using the proposed PPMN to replace the half wavelength off-set TL. In the new structure shown in Fig. 5, two PPMNs are introduced, where PPMN_C replaces the quarter wavelength TL as the impedance inverter while PPMN_P acts as a half wavelength TL to extend the bandwidth of the DPA.

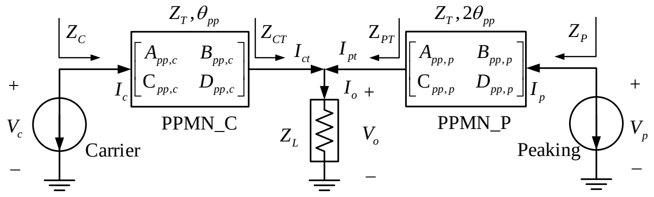

Fig. 5. wideband DPA using PPMNs as impedance inverter and offset element.

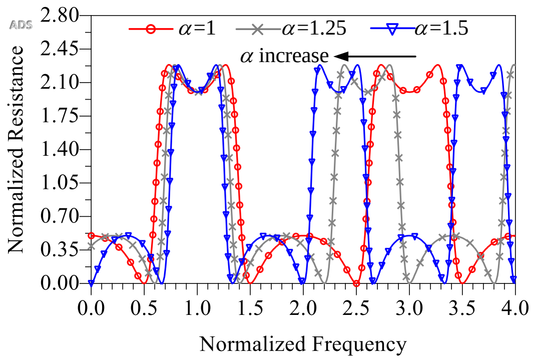

Fig. 6. Simulated resistance at back-off region of wideband DPA using PPMNs as impedance inverter and peaking off-set element for different values of α.

In this configuration, the carrier back-off impedance can be calculated as,

$$Z_{C,bo} = Z_T \frac{1 - tan\theta_{pp,c} tan\theta_{pp,p} + j2tan\theta_{pp,c}}{2 + jtan\theta_{pp,c} + jtan\theta_{pp,p}} \tag{4}$$

To provide the desired wideband performance, the phase characteristic of PPMN_C and PPMN_P must satisfy the similar relationship between the quarter and half wavelength TLs. In this case, we can simply set $\theta_{pp,c} = \theta_{pp}$ and $\theta_{pp,p} = 2\theta_{pp}$. The value of θ_{pp} is defined by (2) and it changes with α. When the value of α changes, the operation frequency of this kind of multi-band DPA will also change. Fig. 6 presents the simulated resistance at back-off region of wideband DPA using PPMNs as impedance inverter and peaking off-set element for different values of α. It can be seen that the bandwidth of each band has been significantly extended in this situation.

From Fig. 6 we can also see that, the bandwidth in each band will decrease as the value of α increases. Assuming the defined bandwidth in each band is calculated within the frequency range where the normalized resistance is larger than 2, the relationship between the bandwidth and α can be obtained. The fractional bandwidth versus the different value of α is shown in Fig. 7, where we can see that, although the fractional bandwidth decreases as α increases, the decreasing trend is gradually reduced. When α increases to 5, the fractional bandwidth is still 13.3%. Meanwhile, the ratio between the center frequencies of the second and first band f_2/f_1 decreases to only 1.4. In order to explain the bandwidth characteristics more clearly, we take $f_1 = 1.8$ GHz as an example. At this situation, when $\alpha = 5$, $f_2 = 2.52$ GHz and the bandwidth in each band is 240 MHz, which is still

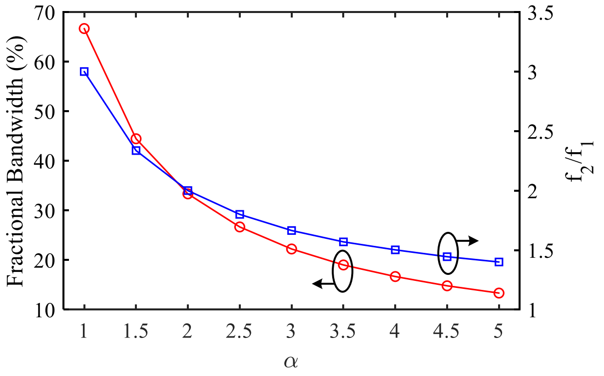

Fig. 7. The fractional bandwidth and the ratio of f_2/f_1 versus the different value of α.

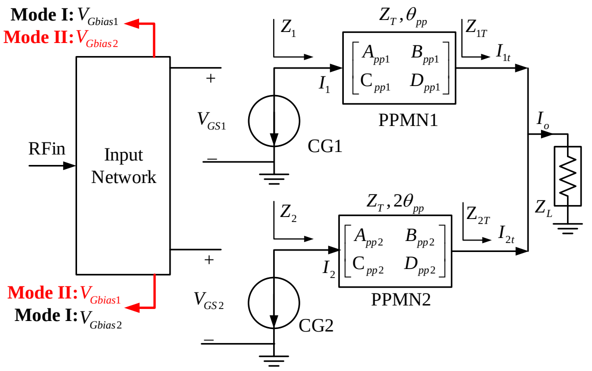

Fig. 8. Block diagram of the proposed dual-mode multi-band DPA.

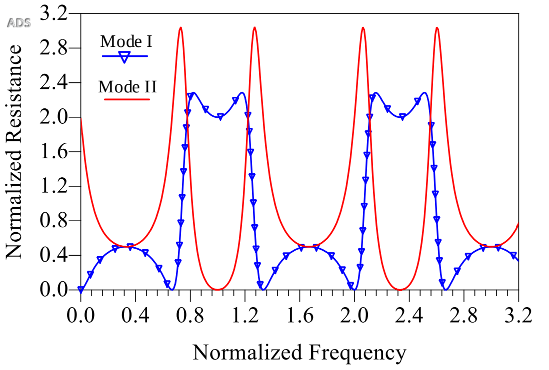

Fig. 9. Simulated carrier resistance at back-off region of proposed dual mode DPA employing PPMNs when $\alpha = 1.5$.

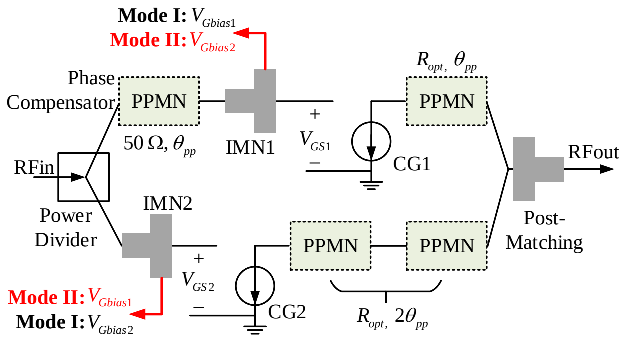

Fig. 10. System architecture of the proposed multi-band DPA.

wider than the required signal bandwidth for 5G applications at sub-6 GHz. In Fig. 7, the ratio between f_2 and f_1 versus the value of α is also given as reference.

B. Increase Band Number Using Reciprocal Gate Bias Dual-Mode Configuration

The above proposed DPA provides a multi-band scheme, but the total bandwidth is still limited. In 5G applications, a large number of frequency bands need be supported. In [28], we presented a design method of dual-mode DPA using reciprocal gate biases, which can extend the bandwidth or increase the bands number without changing the load modulation network. To further increase the bandwidth of the proposed DPA, the same reciprocal gate biases approach can be employed to operate the DPA in two different modes to support a large number of bands. Fig. 8 shows the block diagram of the proposed dual-mode multi-band DPA. The load modulation network of this DPA is the same as the wideband DPA introduced in the previous subsection. Meanwhile, two different DPA modes are set by swapping the gate biases of CG1 and CG2. In Mode I, CG1 is biased with V_{Gbias1} at class-AB mode as the carrier active device while the CG2 is biased with V_{Gbias2} at class-C mode as the peaking active device. In Mode II, the matching networks are the same, but the gate biases of CG1 and CG2 are swapped and thus the carrier and peaking active devices are exchanged, namely, CG1 becomes peaking and CG2 becomes carrier. In this situation, the condition of equal-phase combining at saturation is the same as the wideband DPA mentioned above, which means the impedance condition can be satisfied in the same way. For Mode I, the carrier back-off impedance can be still expressed as,

$$Z_{m1,bo} = Z_T \frac{1 - tan\theta_{pp1} tan\theta_{pp2} + j2tan\theta_{pp1}}{2 + jtan\theta_{pp1} + jtan\theta_{pp2}} \tag{5}$$

where θ_{pp1} and θ_{pp2} are the phase shift of PPMN1 and PPMN2, respectively. Similarly, the carrier back-off impedance for Mode II can be calculated as,

$$Z_{m2,bo} = Z_T \frac{1 - tan\theta_{pp1} tan\theta_{pp2} + j2tan\theta_{pp2}}{2 + jtan\theta_{pp1} + jtan\theta_{pp2}} \tag{6}$$

From (5) and (6), the carrier back-off impedance for Mode I and Mode II can be presented in Fig. 9. For Mode I, the Doherty operation is the same as that mentioned in the previous subsection. For Mode II, the carrier back-off resistance presents similar characteristic as introduced in [28]. Compared with Mode I, the number of bands is doubled in Mode II.

C. System Architecture of Proposed Multi-Band DPA

Moving to real implementation, the theoretical block diagram of the proposed DPA shown in Fig. 8 can be converted into the system architecture shown in Fig. 10. To reduce design complexity, the half-wavelength PPMN2 in the peaking branch is divided into two quarter-wavelength PPMNs, which can be the same as the PPMN1 in the carrier branch. Since

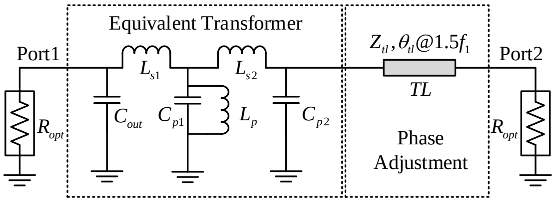

Fig. 11. Proposed PPMN circuits architecture.

the phase shift of PPMN1 is θ_{pp}, two cascaded PPMNs automatically achieve a phase shift of $2\theta_{pp}$ in the peaking branch. Furthermore, as mentioned early, the equal-phase combining condition is required at saturation. Because the PPMNs have the similar characteristics to the TLs, the equal-phase combining condition can be described by using the current relationship between the CG1 and CG2 as,

$$I_{1,sat} = I_{2,sat} \cdot e^{j(\theta_{pp1}-\theta_{pp2})} = I_{2,sat} \cdot e^{-j\theta_{pp}} \tag{7}$$

which means that another PPMN with the phase shift of θ_{pp} is required to be added in the input of CG1 to compensate the phase difference generated by the two PPMNs in the output of CG2. In summary, for the system architecture shown in Fig. 10, four PPMNs are used to achieve the proposed multi-band Doherty operation. Three of them are with the same matching impedance of R_{opt} and phase shift of θ_{pp}. They are employed to build the proposed multi-band load modulation network. Meanwhile, another PPMN with the same phase shift and matching impedance of 50 Ω is used as the phase compensator. Two input matching networks (IMNs) with same structure should be employed to provide wideband gain ability in both Mode I and Mode II. A broadband power divider is required to separate the input power in the target bands. Meanwhile, post-matching network will be employed to transfer the 50 Ω load to $R_{opt}/2$. Two DPA modes can be achieved by swapping the gate biases of CG1 and CG2 without changing the circuits. It should be noticed that, a 3 dB power divider is employed at the input of the proposed architecture to ensure the dual-mode operation. This configuration might reduce the linearity of the proposed DPA to some extent [30], [31].

III. CIRCUIT ARCHITECTURE AND DESIGN EXAMPLES OF PPMN

The most important part for realizing the proposed multi-band DPA is the design of the PPMNs. From Fig. 10, we can see that all four PPMNs can be implemented by using the same circuit architecture. As discussed in Section II, the PPMN should be tunable according to the operation bands requirement, namely, by changing the value of α, specific operation bandwidths of the DPA should be obtained. It is, therefore, very important to find a proper circuit architecture for the PPMN so that it can meet different bandwidth requirements by changing the value of α.

A circuits topology including both lumped and distributed components is proposed here to realize the PPMN, as shown in Fig. 11. This architecture includes an equivalent transformer and a phase adjustment TL. The equivalent transformer provides a larger phase slope compared that with TLs and achieve part of the impedance matching function in the target frequency range that covers all the operation bands in both Mode I and Mode II. Because the required PPMN needs to achieve phase value at specific frequencies, a TL with characteristic impedance close to R_{opt} is added after the equivalent transformer to adjust the phase value of the entire PPMN.

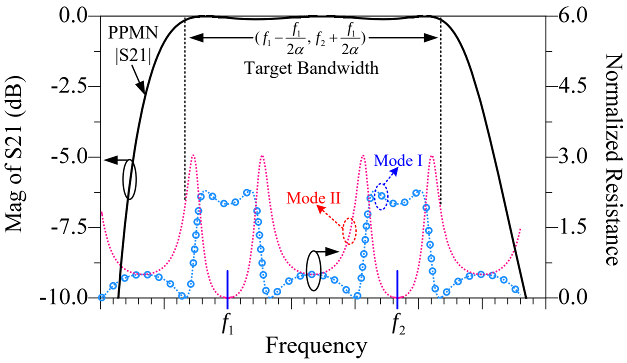

Fig. 12. Desired magnitude of S_{21} of the PPMN.

A. Theoretical Analysis

The ABCD matrix of the proposed PPMN can be calculated using the corresponding matrices of each element shown in Fig. 11 as,

$$\mathbf{A_{PPMN}} = \mathbf{A_{C_{out}}} \mathbf{A_{L_{s1}}} \mathbf{A_{C_{p1}}} \mathbf{A_{L_p}} \mathbf{A_{L_{s2}}} \mathbf{A_{C_{p2}}} \mathbf{A_{TL}} \tag{8}$$

where the corresponding matrices can be expressed as,

$$\mathbf{A_{C_p}} = \begin{bmatrix} 1 & 0 \\ j\omega C_p & 1 \end{bmatrix} \tag{9}$$

$$\mathbf{A_{L_s}} = \begin{bmatrix} 1 & j\omega L_s \\ 0 & 1 \end{bmatrix} \tag{10}$$

$$\mathbf{A_{L_p}} = \begin{bmatrix} 1 & 0 \\ 1/(j\omega L_p) & 1 \end{bmatrix} \tag{11}$$

$$\mathbf{A_{TL}} = \begin{bmatrix} \cos\theta_{tl} & jZ_{tl}\sin\theta_{tl} \\ j(\sin\theta_{tl})/Z_{tl} & \cos\theta_{tl} \end{bmatrix} \tag{12}$$

Let's assume $\mathbf{A_{PPMN}}$ has the expression of

$$\mathbf{A_{PPMN}} = \begin{bmatrix} A_P & B_P \\ C_P & D_P \end{bmatrix} \tag{13}$$

Therefore, the forward transmission coefficient S_{21}^p of the PPMN can be calculated as,

$$S_{21}^p = \frac{2R_{opt}}{A_P R_{opt} + B_P + C_P R_{opt}^2 + D_P R_{opt}} \tag{14}$$

For the PPMN, the magnitude and phase of S_{21}^p should satisfy the specific conditions based on the impedance requirements of the proposed DPA operation. However, it is difficult to obtain an analytical solution of the required PPMN directly from (14). To obtain the required element values, parameter optimization method is adopted. The optimal goal function should be decided based on the characteristics of the PPMN.

TABLE I
OPTIMIZED PPMN CIRCUITS PARAMETERS FOR DIFFERENT VALUES OF α WHEN R_{opt} = 62 Ω AND f_1 = 2 GHZ

α	C_{out}	C_{p1}	C_{p2}	L_{s1}	L_{s2}	L_p	Z_{tl}	θ_{tl}
N/A	pF	pF	pF	nH	nH	nH	Ω	°
1.25	0.8	1.27	0.45	1.65	1.44	5.59	51.9	54.1
1.5	0.8	1.51	0.57	1.91	1.77	4.75	54.3	53.7
1.75	0.87	1.97	0.81	2.03	1.95	3.34	56.5	47.6
2	1.07	2.71	0.99	1.97	1.89	2.19	55.3	44.8

For the PPMN shown in Fig. 11, the magnitude of S_{21}^p needs to be as close to 1 as possible to provide the required impedance value R_{opt} within the target bandwidth which includes all the operation bands in both Mode I and Mode II, as illustrated in Fig. 12. In addition, the slope of S_{21}^p phase α must be within the same target bandwidth to guarantee the proposed multi-band Doherty operation. At the same time, the phase value of S_{21}^p at one selected frequency should be set as a reference, thus the entire S_{21}^p phase characteristics can be determined. Therefore, the optimal goals to obtain the element values can be written as,

$$\begin{cases} |S_{21}^p| \rightarrow 1, f_1 - \dfrac{f_1}{2\alpha} \leq f \leq f_2 + \dfrac{f_1}{2\alpha} \\ \angle S_{21}^p \rightarrow -\pi, f = (f_1 + f_2)/2 \\ \dfrac{d\angle S_{21}^p}{df} \rightarrow \alpha, f_1 - \dfrac{f_1}{2\alpha} \leq f \leq f_2 + \dfrac{f_1}{2\alpha} \end{cases} \tag{15}$$

The condition (15) describes the optimal goals of the proposed PPMN when there are two target bands in Mode I and four target bands in Mode II. f_1 and f_2 are the center frequencies of the two bands in Mode I, $(f_1 - \frac{f_1}{2\alpha}, f_2 + \frac{f_1}{2\alpha})$ is the target bandwidth of the proposed PPMN which is defined based on the edge frequency of Mode II when $Z_{m2,bo} = 2R_{opt}$. Based on equation (2), the relationship between f_1 and f_2 can be expressed as $f_2 = f_1(\alpha + 2)/\alpha$. Besides, the reference phase of the PPMN is set to $-\pi$ at $(f_1 + f_2)/2$ and the reference frequency to measure θ_{tl} is set to $1.5f_1$. Based on the above analysis, we can design the proposed PPMNs.

B. Optimization Examples

Some examples of the proposed PPMN in different conditions are given in this subsection to illustrate the practicality of the design. Table I shows the optimization results for different values of α when R_{opt} = 62 Ω and f_1 = 2 GHz. This example is optimized for the case that uses a 6 Watts commercial GaN device. Considering the drain to source capacitor of the device C_{ds} is usually absorbed into the PPMN, the value of C_{out} is set to a range that is close to C_{ds} in a practical device during the optimization process. It is worth mentioning that the proposed PPMN is equivalent to a normal TL when $\alpha = 1$ while the target bandwidth can reach one octave when $\alpha > 2$.

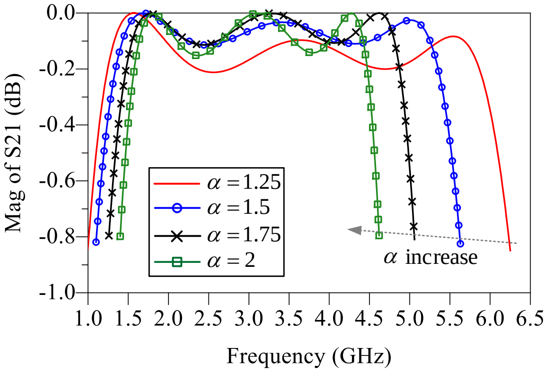

Fig. 13. Simulated magnitude of S_{21} of the proposed PPMN for different values of α when R_{opt} = 62 Ω and f_1 = 2 GHz.

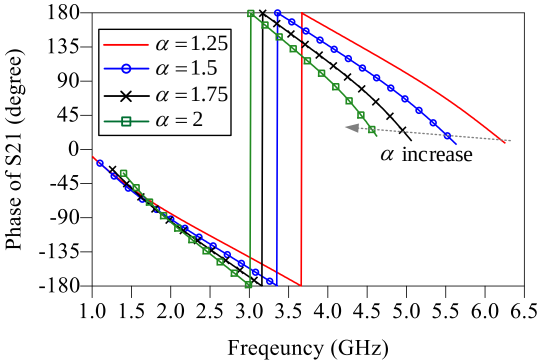

Fig. 14. Simulated phase of S_{21} of the proposed PPMN for different values of α when R_{opt} = 62 Ω and f_1 = 2 GHz.

TABLE II
OPTIMIZED PPMN CIRCUITS PARAMETERS FOR DIFFERENT VALUES OF α WHEN R_{opt} = 32 Ω AND f_1 = 1.5 GHZ

α	C_{out}	C_{p1}	C_{p2}	L_{s1}	L_{s2}	L_p	Z_{tl}	θ_{tl}
N/A	pF	pF	pF	nH	nH	nH	Ω	°
1.25	1.28	2.58	1.44	1.39	1.25	7.86	30.2	51.6
1.5	1.89	3.94	1.81	1.38	1.34	3.41	30.0	45.9
1.75	2.34	5.37	2.19	1.37	1.32	2.13	29.1	45.7
2	2.76	7.00	2.56	1.36	1.30	1.50	28.5	44.8

Table I presents the element values when α is between 1 to 2, and the magnitude and phase of S_{21}^p verse different values of α are presented in Fig. 13 and Fig. 14, respectively, where we can see that, when α increases, the total optimization bandwidth becomes slightly narrower, while the phase of the PPMN at f_1 and f_2 is close to the required value $-\pi/2$ or $\pi/2$. This phase characteristic guarantees the proposed Doherty operation. When α increases from 1.25 to 2, f_2 changes from 5.2 GHz to 4.0 GHz. The results shown in Fig. 13 and Fig. 14 prove that the proposed PPMN topology and optimization method can successfully obtain the required network characteristic and the spacing between f_1 and f_2 can be easily adjusted.

To further verify whether the proposed PPMN architecture and its optimization method are workable under different R_{opt} conditions and at different frequency ranges, circuits

TABLE III
OPTIMIZED PPMN CIRCUITS PARAMETERS FOR DIFFERENT VALUES OF α WHEN R_{opt} = 16 Ω AND f_1 = 1.5 GHZ

α	C_{out}	C_{p1}	C_{p2}	L_{s1}	L_{s2}	L_p	Z_{tl}	θ_{tl}
N/A	pF	pF	pF	nH	nH	nH	Ω	°
1.25	2.66	4.64	2.11	0.74	0.72	4.32	15.6	53.1
1.5	3.00	7.26	3.94	0.74	0.70	1.88	15.7	47.3
1.75	4.67	10.77	4.48	0.69	0.68	1.07	15	44.1
2	5.44	13.85	5.24	0.69	0.67	0.77	15	42.3

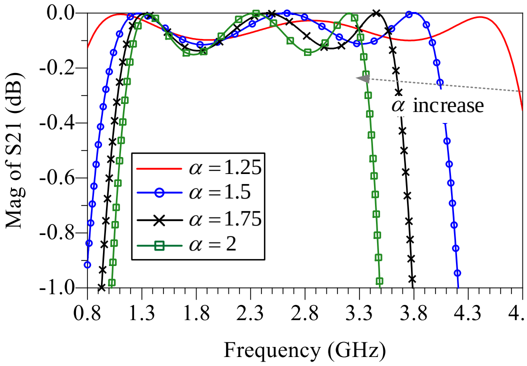

Fig. 15. Simulated magnitude of S_{21} of the proposed PPMN for different values of α when R_{opt} = 32 Ω and f_1 = 1.5 GHz.

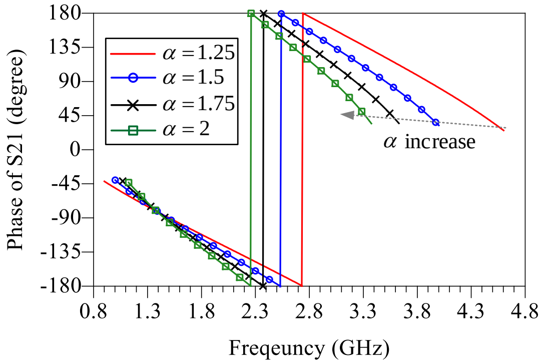

Fig. 16. Simulated phase of S_{21} of the proposed PPMN for different values of α when R_{opt} = 32 Ω and f_1 = 1.5 GHz.

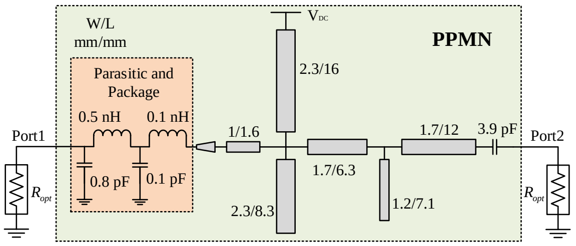

Fig. 17. Schematic of the proposed PPMN.

TABLE IV
OPTIMIZED PPMN CIRCUITS PARAMETERS FOR THE PROPOSED DESIGN

α	C_{out}	C_{p1}	C_{p2}	L_{s1}	L_{s2}	L_p	Z_{tl}	θ_{tl}
N/A	pF	pF	pF	nH	nH	nH	Ω	°
1.86	0.8	2.15	0.97	2.16	2.01	2.91	58	45.7

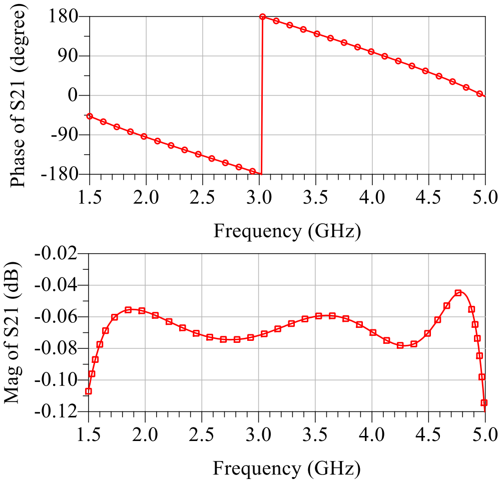

Fig. 18. Simulated phase and magnitude of S_{21} of the proposed PPMN.

parameters are optimized when $R_{opt} = 32$ Ω and $R_{opt} = 16$ Ω, while f_1 is set to 1.5 GHz at the same time. These two examples are designed for using 10 Watts and 25 Watts commercial GaN devices. Table II and Table III summarize the optimized parameter values of each component when $R_{opt} = 32$ Ω and $R_{opt} = 16$ Ω, respectively. In these two situations, when α increases from 1.25 to 2, f_2 changes from 3.9 GHz to 3.0 GHz. The related magnitude and phase of S^p_{21} under the condition of $R_{opt} = 32$ Ω are presented in Fig. 15 and Fig. 16, respectively. It can be seen that the phase characteristic also satisfy the required condition. Due to the similarity of the features, the magnitude and phase of S^p_{21} under the situation when $R_{opt} = 16$ Ω are not given here.

As can be seen from the above analysis, the proposed PPMN architecture has a certain flexibility to achieve the desired phase characteristics within a wide bandwidth.

IV. DESIGN OF DUAL-MODE 6-BAND DPA USING THE PROPOSED ARCHITECTURE

In this section, we will design a 6-band DPA to validate the proposed architecture and design methodology. Based on the analysis in section III, the operation bands are directly related to the value of α. Therefore, to design the required PPMNs, the value of α needs to be determined first. For a 6-band DPA employing the proposed architecture, two bands in Mode I and four bands in Mode II will be achieved. At the two centre frequencies of Mode I, i.e., f_1 and f_2, the value of θ_{pp} is fixed, which are $\theta_{pp,f_1} = -\pi/2$ and $\theta_{pp,f_2} = -3\pi/2$. Therefore, the value of α can be calculated from (2) based on the center operation frequency of Mode I. In this design, the values of f_1 and f_2 are set to 2.0 and 4.15 GHz, respectively.

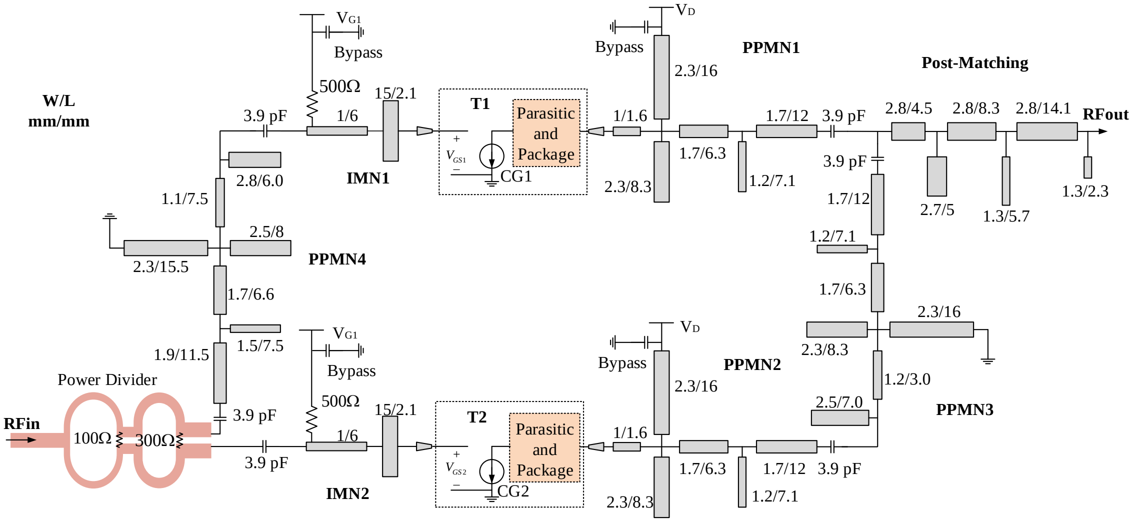

Fig. 19. Schematic of the proposed multi-band DPA employing PPMNs.

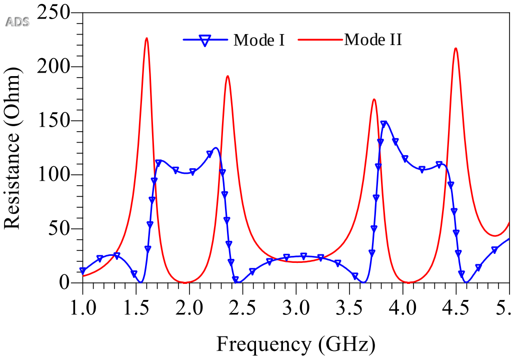

Fig. 20. Simulated back-off resistance for Mode I and Mode II versus frequency.

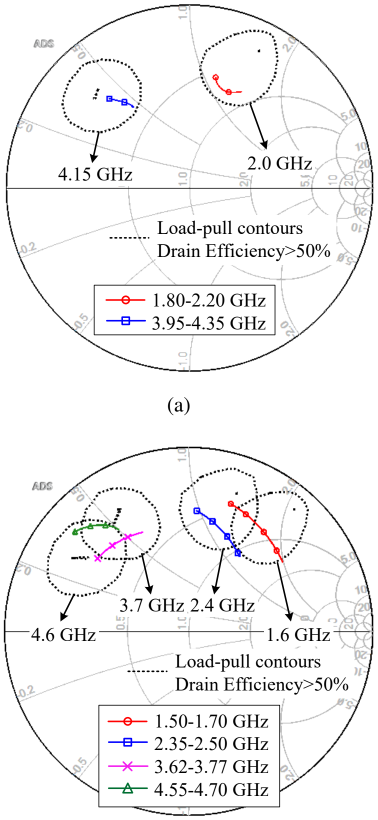

(a)

(b)

Fig. 21. Simulated back-off impedance compared with load-pull data in (a) Mode I (b) Mode II.

Therefore the value of α is 1.86. Once α is determined, the four center frequencies of Mode II bands can be obtained, which are 1.564, 2.436, 3.714 and 4.586 GHz. Meanwhile, the phase characteristic of the target PPMN is also determined.

The matching target of the proposed PPMN is to obtain R_{opt} while achieving the phase characteristic within the target bandwidth covering all the bands at the same time. In this work, GaN HEMTs CGH40006s from Wolfspeed are used as the active devices, which have the R_{opt} of 62 Ω. The parasitic and package parameters obtained from the turn-off S-parameters in [28] is also used here. The circuit architecture and optimization method introduced in Section III are employed to realize the required PPMN with $\alpha = 1.86$.

Firstly, we use the circuit topology shown in Fig. 11. The values of these circuit element are listed in Table IV. Secondly, C_{out} is used to absorb the drain to source capacitor of the proposed device and the package inductor is also absorbed in L_{s1} at the same time. It should be noticed that there is another package capacitor which is not absorbed, so the initial PPMN need be optimized to some extent. After obtaining the parasitic and package absorbed PPMN circuits, we transfer all the lumped components to distributed forms (TLs) based on the transformation method introduced in [32]–[34] except the parasitic and package part. Fig. 17 presents the schematic of the proposed PPMN, which absorbs the parasitic and package parameters of the used transistor. The values of the parasitic and package parameters are also shown in Fig. 17. Fig. 18 presents the S21 of the designed PPMN. It can be seen that the

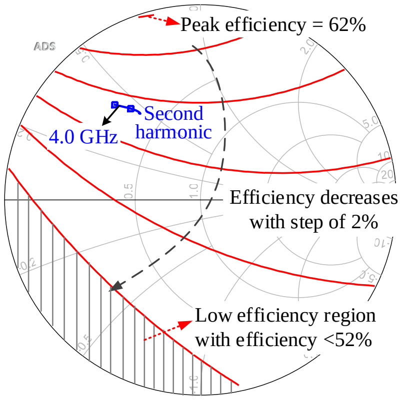

Fig. 22. Second harmonic impedance of lower band in Mode I and back-off efficiency contours of the second harmonic load-pull simulation at 2 GHz.

impedance matching target is well achieved from 1.5 to 5 GHz while the phase characteristic also satisfies the requirements.

After designing the PPMN, we can use it to build the proposed multi-band DPA. Fig. 19 presents the schematic of the proposed DPA. Four PPMNs are employed to realize different functional elements for the proposed DPA and input matching networks (IMNs) with same size are designed for both CG1 and CG2 branches. In CG1 branch, the designed PPMN1 is employed as the impedance inverter for Mode I, and two PPMNs (PPMN2 and PPMN3) are used as the off-set element in CG2 branch to realized the phase shift of $2\theta_{pp}$. To provide the phase compensation for all the operation bands, PPMN4, which has the same phase characteristic as PPMN3, is added at the input of IMN1. The matching impedance of PPMN4 is 50 Ω. In PPMN3 and PPMN4, TL structure is used to instead of the parasitic and package components shown in Fig. 17. A post-matching network covering all the target bands is then designed using high-order low-pass TL topology to realize the impedance matching from 50 Ω load to $R_{opt}/2$. Furthermore, to provide the power division at all the operation frequencies, a 2-stage broadband power divider is employed. All the above mentioned circuits are realized on a 31 mil Rogers 5880 substrate and simulated using Keysight ADS momentum. The specific size of the used TLs are also shown in Fig. 19.

Fig. 20 presents the simulated back-off resistance at CG plane in Mode I and Mode II versus frequency. It can be seen that the back-off resistance is close to the theoretical value, which means that the multi-band Doherty operation can be achieved. To present the achieved matching results more clearly, Fig. 21 shows the simulated back-off impedance at the transistor package plane compared with load-pull data in both Mode I and Mode II. The load-pull data is obtained at the back-off output power level. We can see that, the back-off impedance is almost within the high efficiency contours in all the operation bands. The peak efficiency of the efficiency contours is higher than 62% as shown in Fig. 21.

For the proposed design, some of the second harmonic frequencies of the lower frequency band overlap with the higher frequency band in Mode I, which means the second harmonic impedance in the lower frequency band is not optimal. This will decrease the efficiency performance of the proposed DPA to some extent at the related frequencies. Nevertheless, this impact is not severe. Here, we use the second harmonic load-pull data at 2 GHz of the used device to illustrate this issue. Fig. 22 presents the back-off efficiency contours of the second harmonic load-pull simulation at 2 GHz. It can be seen that, when the second harmonic impedance is in the low efficiency region, the efficiency will be reduced. Nevertheless, the realized second harmonic impedance, which is the obtained matching impedance at 4 GHz, is actually far from the low efficiency region. This level of reduction is acceptable for an ultra wideband DPA. In addition, the mentioned frequency overlapping may compromise the performance in case of concurrent dual-band transmission. In practical operation, this issue can be avoided if we do not simultaneously transmit the signals at two exactly overlapped bands. For instance, if we transmit 60 MHz signal at 1.9 GHz and another 60 MHz signal at 4.1 GHz concurrently, the two signals will not overlap with each other. It should be noticed that, the specific design in this work is just an example to validate the proposed method. As shown in Fig. 6, the two bands in Mode I can be chosen without overlap.

The simulated drain efficiency and gain of the proposed DPA versus output power in Mode I and Mode II are shown in Fig. 23 and Fig. 24, respectively. In Mode I, two operation bands of 1.8-2.2 GHz and 3.95-4.35 GHz are obtained. In these two bands, 6 dB drain efficiency of 49.6%-57.4% and

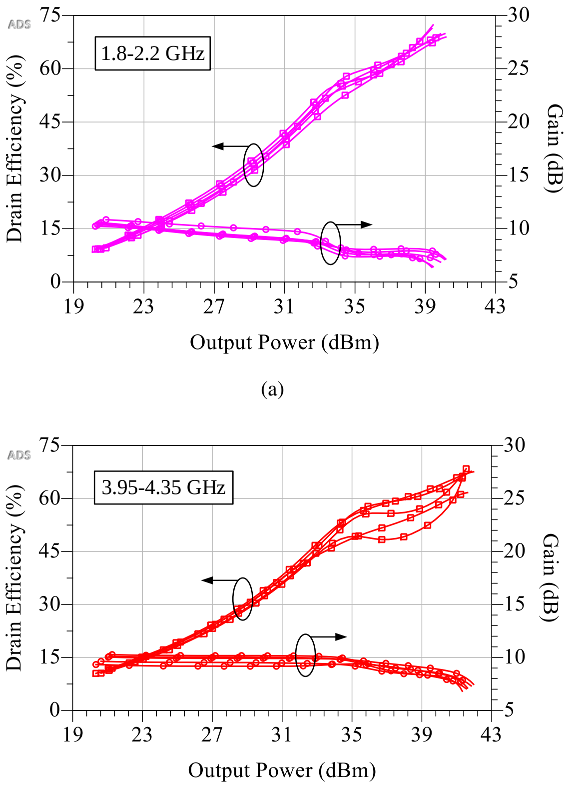

(a)

(b)

Fig. 23. Simulated drain efficiency and gain of the proposed DPA versus output power in Mode I at (a) 1.8-2.2 GHz (b)3.95-4.35 GHz.

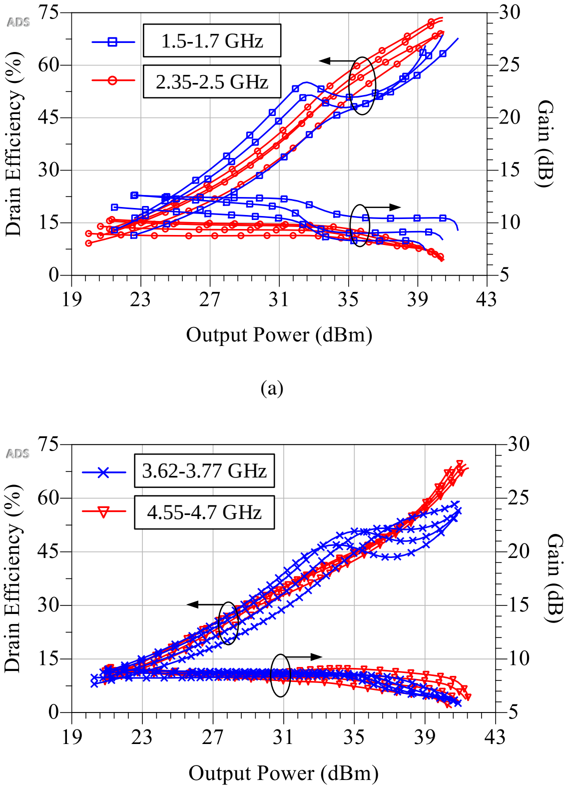

(a)

(b)

Fig. 24. Simulated drain efficiency and gain of the proposed DPA versus output power in Mode II at (a) 1.5-1.7/2.35-2.5 GHz (b)3.62-3.77/4.55-4.7 GHz.

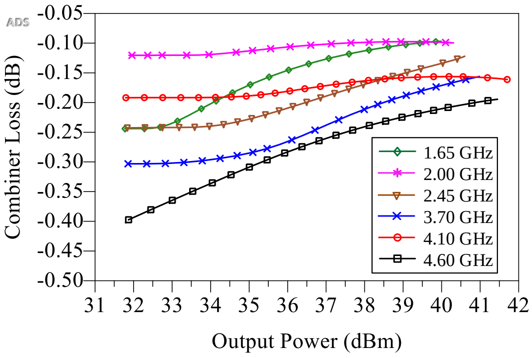

Fig. 25. Simulated loss of the combiner versus output power at different operation frequencies.

maximum efficiency of 61.7%-72.3% are achieved with peak output power of 39.5 to 41.9 dBm. In Mode II, four operation bands of 1.5-1.7 GHz, 2.35-2.5 Ghz, 3.62-3.77 GHz and 4.55-4.7 GHz are achieved. In these four bands, 6 dB drain efficiency of 44.1%-53.5% and maximum efficiency of 65.4%-73.5% are achieved with peak output power of 39.6 to 41.4 dBm. The simulated loss of the power combiner at some operation frequencies versus the output power is presented in Fig. 25. It can be found that the loss in Mode I is smaller than that in Mode II at OBO. The combining loss can partially explain why the power amplifier is less efficient at certain operating frequencies. Fig. 26 shows the simulated output phase versus output power at different operation frequencies, where we can see that, the phase distortion in Mode I is smaller compared to that in Mode II. From the above results we can find, the Doherty operation in Mode II is compromised and this non-ideal characteristic affects both efficiency and linearity performance in Mode II.

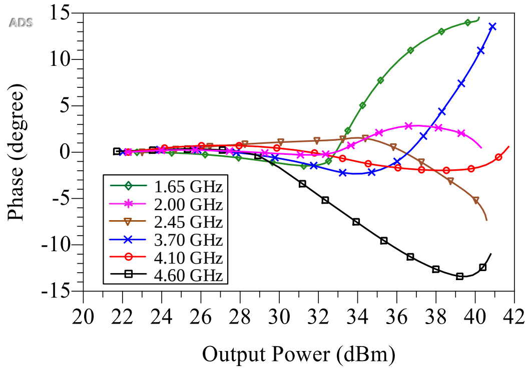

Fig. 26. Simulated output phase versus output power at different operation frequencies.

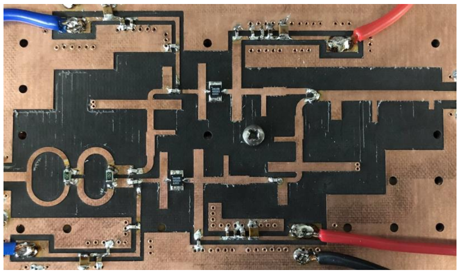

Fig. 27. Fabricated circuits of the proposed DPA.

V. EXPERIMENTAL RESULTS

The circuit photograph of the fabricated DPA is shown in Fig. 27. The DPA was measured under both continuous-wave (CW) and wideband modulated signal stimulation at different operation frequency bands. Some of the designed frequencies with high back-off efficiency slightly shifted from simulation due to fabrication variations. The final measured operation bands were 1.8-2.2 GHz and 3.9-4.3 GHz in Mode I, 1.52-1.72 GHz, 2.38-2.53 GHz, 3.67-3.82 GHz and 4.53-4.68 GHz in Mode II. To show the multi-band feature of the implemented DPA, performance at peaking output power and back-off region were also measured from 1 GHz to 5 GHz with 0.1 GHz step. In the measurements, drain biases of 28 V and carrier quiescent current of 80 mA were set for the two devices in both Mode I and Mode II while the peaking gate biases were set to -6.3 V in Mode I and -5.7 V in Mode II to obtain better better performance.

A. Measurements with CW Signal

The measured small signal gain of the proposed DPA from 1 to 5 GHz is presented in Fig. 28 where six operation bands can

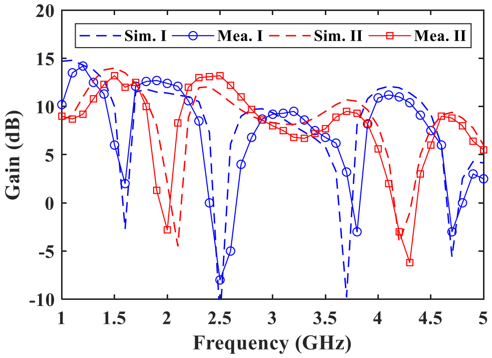

Fig. 28. Measured and simulated small signal gain of the proposed dual-mode multi-band DPA versus operation frequency.

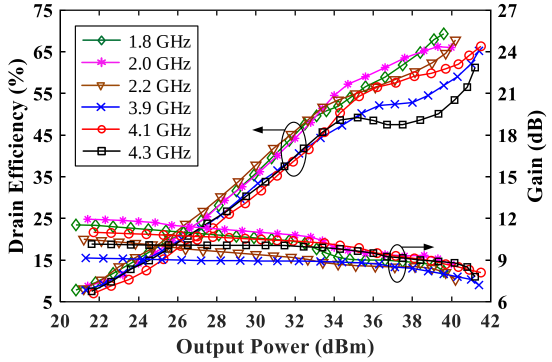

Fig. 29. Measured drain efficiency and gain of the proposed DPA in Mode I versus output power.

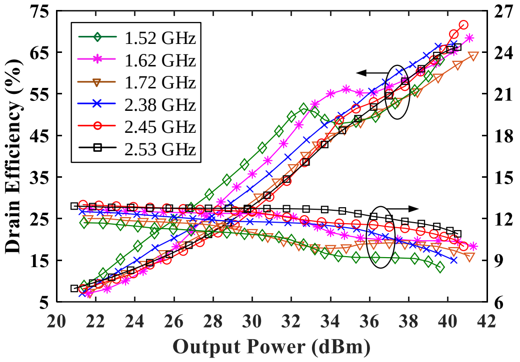

Fig. 30. Measured drain efficiency and gain of the proposed DPA in the lower frequency bands of Mode II versus output power.

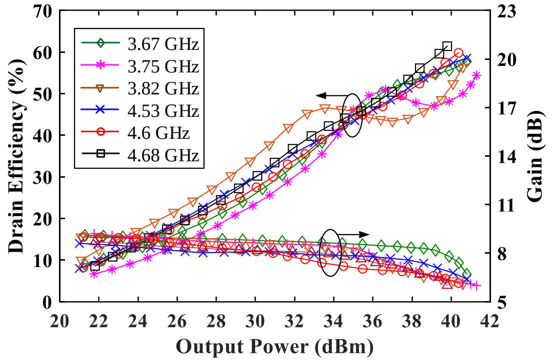

Fig. 31. Measured drain efficiency and gain of the proposed DPA in the upper frequency bands of Mode II versus output power.

be observed. For these six bands, the measured small signal gain changes from 8.7 to 13.5 dB. Besides, it can be seen from Fig. 28 that each designed band has wider than hundred MHz gain bandwidth, which makes the proposed DPA possible for supporting wide signal bandwidth. The simulated small signal gain is also given in Fig. 28 as comparison.

The measured drain efficiency and gain of the proposed DPA in Mode I versus output power is shown in Fig. 29. The achieved bands with high back-off efficiency are 1.8-2.2 GHz and 3.9-4.3 GHz. Drain efficiency of 61.2%-69.3% and 49.2%-54.5% is achieved at the peak output power and 6 dB back-off region, respectively. The corresponding power added efficiency (PAE) is 51.1%-58.8% at saturation and 43.9%-48.9% at 6 dB back-off. The measured maximum output power is within the range of 39.6 dBm to 41.5 dBm in Mode I. Each band in Mode I can achieve 400 MHz bandwidth with higher than 49.2% drain efficiency at 6 dB back-off. Fig. 30 and Fig. 31 present the measured drain efficiency and gain of the proposed DPA in Mode II versus output power. The achieved four bands with high back-off efficiency are 1.52-1.72 GHz, 2.38-2.53 GHz, 3.67-3.82 GHz and 4.53-4.68 GHz. Drain efficiency of 54.4%-71.3% and 42.2%-56.7% is achieved at the peak output power and 6 dB back-off region, respectively. The corresponding PAE is 40.7%-64.4% at saturation and 35.4%-50.5% at 6 dB back-off. The measured maximum output power is within the range of 39.6 dBm to 41.3 dBm in Mode II. At least 150 MHz bandwidth can be achieved with higher than 42% 6 dB back-off drain efficiency for each band in Mode II.

From the above CW measurement results we can see, the fabricated DPA realized the proposed multi-band function. The Doherty operation is more obvious in Mode I. At some frequencies in Mode II, especially 2.38-2.53 GHz and 4.53-4.68 GHz bands, the Doherty operation is not so obvious. This might be caused by several factors such as the fundamental impedance mismatch and non-perfect harmonic control. Besides, because the targeted bands of the proposed DPA are distributed in a very wide frequency range, the related gain can vary at different frequencies. This may lead the peaking amplifier is turned on earlier. In this situation, the carrier PA has not been driven to voltage saturation at back-off while the peaking PA already begins to generate power. The back-off efficiency thus will reduce to some extent and the Doherty behavior will become not obvious. It can also be found that the back-off impedance in Mode II changes significantly with different frequencies. In theory, different bias condition should be set to ensure the perfect load modulation. However, we keep the gate bias constant in each mode to reduce the system complexity. In this situation, the efficiency performance at back-off will also be affected. Moreover, the PPMNs used in the peaking branch are also not perfect. This means the output impedance of the peaking branch at back-off deviates from the theoretical value, this leads to power leakage from

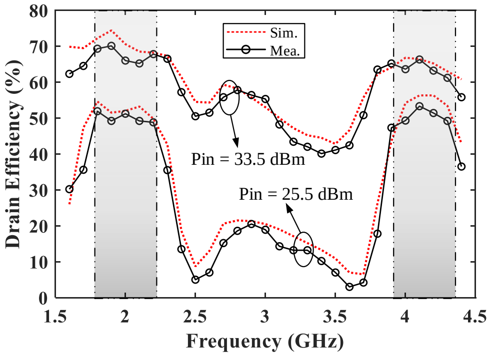

Fig. 32. Simulated and measured drain efficiency at different input power levels versus frequency in Mode I (gray-shaded areas indicating operation bands).

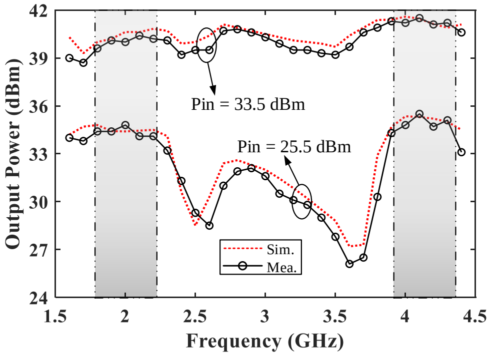

Fig. 33. Simulated and measured output power at different input power levels versus frequency in Mode I (gray-shaded areas indicating operation bands).

the carrier to the peaking branch at some frequencies and thus decrease the back-off efficiency and output power. In Fig. 25, the combining loss of the proposed DPA is different at different operation frequencies, which proves this non-ideality to some extent. Nevertheless, the achieved back-off efficiency is still comparable with other reported dual-band or multi-band DPAs.

To better present the multi-band performance of the proposed DPA, the drain efficiency and related output power versus frequency at different input power levels in both Mode I and Mode II are given. Fig. 32 shows the drain efficiency when the input power equals 33.5 dBm and 25.5 dBm, respectively. It can be seen that higher efficiency performance is achieved in the two target bands. The dual-band characteristic in Mode I is obvious, especially for the back-off efficiency. The simulated drain efficiency is also given in Fig. 32 for comparison. The simulated and measured output power in Mode I when driven by the same input power level is shown in Fig. 33. Besides, Fig. 34 presents the simulated and measured drain efficiency performance at different input power levels. Input power of 35 dBm and 26 dBm is used to better present the quad-band characteristic considering the different gain performance in Mode II. It can be also seen that higher efficiency performance is achieved in the four target bands. Similarly, the simulated and measured output power in Mode II when driven by the same input power level is shown in Fig. 35.

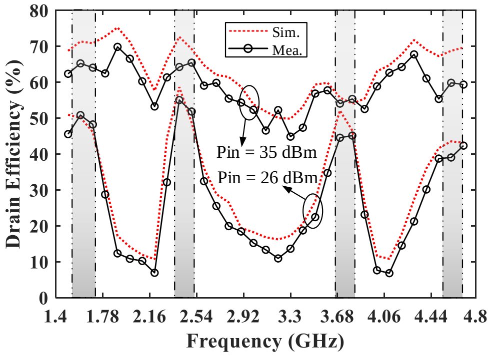

Fig. 34. Simulated and measured drain efficiency at different input power levels versus frequency in Mode II (gray-shaded areas indicating operation bands).

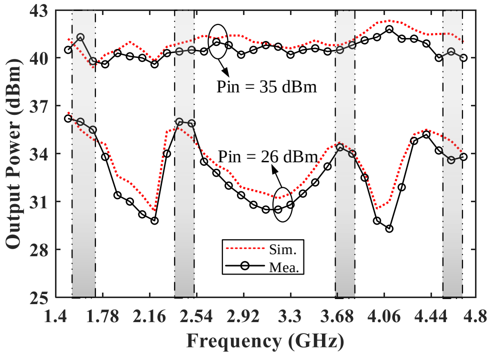

Fig. 35. Simulated and measured output power at different input power levels versus frequency in Mode II (gray-shaded areas indicating operation bands).

TABLE V
PERFORMANCE OF THE PROPOSED DPA UNDER STIMULATION OF A 5 CARRIER 100 MHZ MODULATED SIGNAL WITH 7.7 DB PAPR

Freq (GHz)	Average Pout (dBm)	Average DE (%)	ACPR w/o DPD (dBc)	ACPR w/ DPD (dBc)
1.65	32.8	50.1	-25.5/-21.5	-51.6/-50.5
1.95	32.9	47.3	-21.4/-24.1	-49.8/-53.3
2.45	33.0	42.1	-23.6/-21.8	-51.3/-50.1
3.75	33.2	35.5	-24.2/-22.9	-51.2/-50.3
4.1	33.5	45.6	-25.0/-20.8	-51.1/-50.4
4.6	33.1	36.9	-26.9/-26.6	-49.3/-48.9

B. Measurements with Modulated Signal

1) Single-carrier measurements: To evaluate the performance of the proposed DPA when driven by wideband modulated signals, a 5-carrier 100 MHz OFDM signal with 7.7 dB PAPR was employed to test the DPA at 1.65/1.95/2.45/3.75/4.1/4.6 GHz, respectively. Digital predistortion (DPD) is also performed to improve the linearity of the DPA. A non-parametric iterative learning control based DPD method [35] was adopted, which iteratively adjusts the

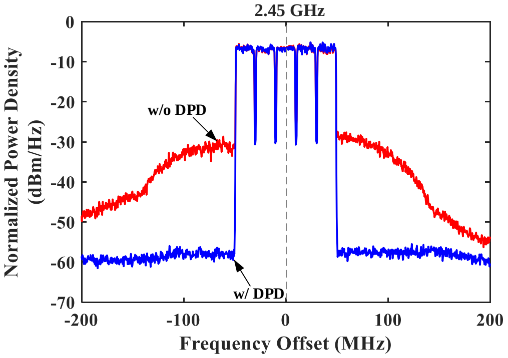

Fig. 36. Output spectrum of the proposed DPA at 2.45 GHz with and without DPD linearization.

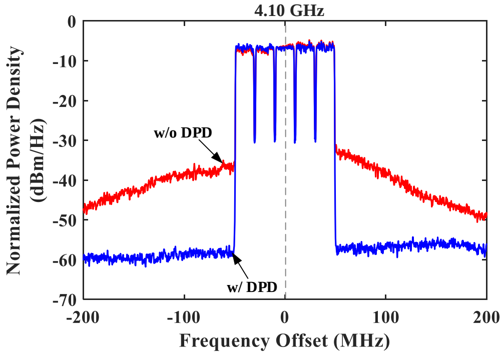

Fig. 37. Output spectrum of the proposed DPA at 4.1 GHz with and without DPD linearization.

predistorted signal to achieve an ideal linear response at PA output. Fig. 36 and Fig. 37 present the output spectrum with and without DPD linearization under the stimulation of the 100 MHz signal at 2.45 GHz and 4.1 GHz. It can be seen the ACPR can be improved to better than -50 dBc after DPD is performed.

To better present the performance of the fabricated DPA under wideband modulated signal stimulation, the average output power, average drain efficiency and the ACPR with and without DPD linearization are summarized in Table V. The proposed DPA achieves average drain efficiency of 35.5% to 50.1% with about 33 dBm average output power at the designed operation frequencies. The corresponding average PAE changes from 30.5% to 44.8%. Better than -21 dBc ACPR is achieved by the DPA without DPD and improved to better than -48.9 dBc after DPD is performed.

2) Concurrent measurements: The proposed DPA was also measured under dual-band concurrent signal stimulation in both Mode I and Mode II. Concurrent dual-band Modulated signal with 7 dB PAPR was employed in this measurement. The signal bandwidth at each band was set to 20 MHz for all the following concurrent measurements. To validate the performance of the proposed DPA, it was tested under different setups by changing the carrier frequency and frequency spacing between the two bands. Different frequency spacing, i.e., 300 MHz, 750 MHz, 1300 MHz and 2200 MHz were adopted in the test. During the measurement, the average

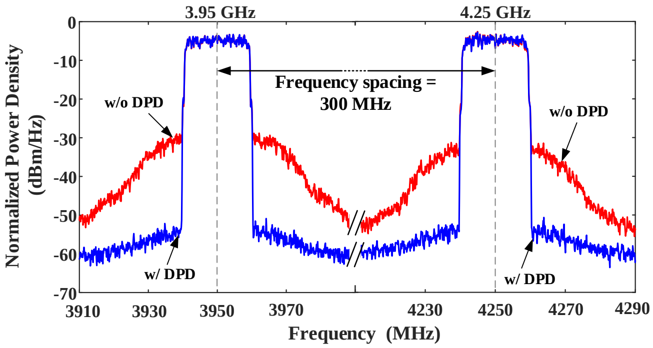

Fig. 38. Output spectrum in Mode I with and without DPD linearization under dual-band concurrent signal stimulation with 300 MHz frequency spacing.

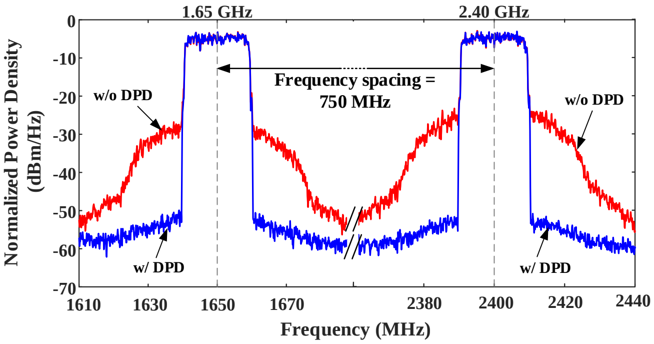

Fig. 39. Output spectrum in Mode II with and without DPD linearization under dual-band concurrent signal stimulation with 750 MHz frequency spacing.

output power of the two frequency bands was kept almost equal. Dual-band DPD was also performed to linearize the DPA under concurrent operation, where the signals of the two bands were captured and time-aligned separately before DPD model extraction.

When the frequency spacing is 300 MHz, the dual-band signal was set within the higher frequency band of Mode I. The center frequencies of the two signals are 3.95 GHz and 4.25 GHz. Fig. 38 resents the corresponding output spectrum. Average drain efficiency of 35.8% was achieved in this configuration with around 30 dBm output power at each band. The ACPRs at these two bands were improved from -28 dBc to better than -50 dBc. Similarly, Fig. 39 and Fig. 40 present the output spectrum in Mode II under dual-band concurrent signal stimulation with 750 MHz and 1300 MHz frequency spacing. The center frequencies of the two signals were 1.65/2.4 GHz and 2.45/3.75 GHz. The average output power at each band was around 29.5 dBm. Average drain efficiency of 41.0% and 34.1% was achieved, respectively. In this situation, the ACPR was better than -25 dBc without DPD and improved to better than -49 dBc after DPD. The DPA was also measured using dual-band signal with frequency spacing of 2200 MHz at center frequencies 1.9 GHz and 4.1 GHz. Due to the limitation of the measurement set-up, the DPD was not performed in this situation and thus the output spectrum is not given here. Average drain efficiency of 34.8% was achieved

TABLE VI
PERFORMANCE COMPARISON OF RECENTLY PUBLISHED MULTI-BAND/BROADBAND DPAS

Ref. (Year)	Type	N_{bands}	Frequency (GHz)	Fmax/Fmin	Pmax (dBm)	Gain (dB)	η_{sat} (%)	η_{6dB} (%)
[6] 2016	Dual-band	2	1.8/2.6	1.44	43.7-43.9	10.5-12.1	60-72	51-63
[7] 2014	Dual-band	2	0.85/2.33	2.74	42.5-44.0	13-19	53-59	46-47
[8] 2016	Quad-band	4	0.73/1.65/2.67/3.57	4.89	41.7-42.5	6-19	52.7-73.1	44.6-58.9
[10] 2017	Reconfigurable	4	1.5/2.14 or 1.85/2.35	1.57	42.4-43.2	10-13	62-70	52-56
[12] 2013	Quad-band	4	0.95/1.5/2.14/2.65	2.79	41.8-44.2	7-12	43-61	32-56
[25] 2018	Broadband	N/A	1.8-3.8 (continuous)	2.11	44.3-46.5	7.6-10.8	42-62	41-51
[26] 2017	Broadband	N/A	1.8-3.8 (continuous)	2.11	42.0-44.0	7.5-11	46-70	33-49
[36] 2014	Broadband	N/A	1.05-2.55 (continuous)	2.43	40.0-42.0	9-10	45-83	35-58
This Work	Dual-Mode Six-band	Mode I:2	1.8-2.2/3.9-4.3	3.07	39.6-41.5	9.1-12.7	61.2-69.3	49.2-54.5
		Mode II:4	1.52-1.72/2.38-2.53/ 3.67-3.82/4.53-4.68		39.6-41.3	8.7-13.5	54.4-71.4	42.2-56.7

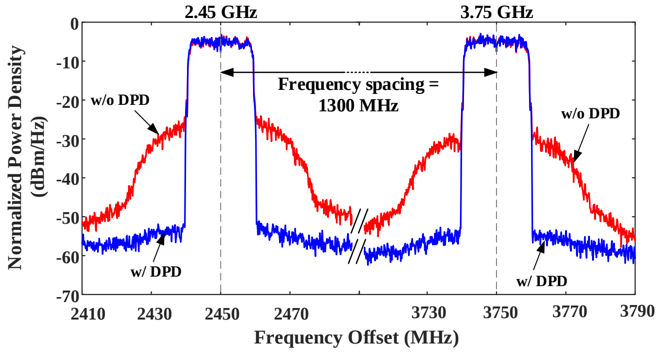

Fig. 40. Output spectrum in Mode II with and without DPD linearization under dual-band concurrent signal stimulation with 750 MHz frequency spacing.

with average output power of 30 dBm at each band. The ACPR was better than -24 dBc at 1.9 GHz and better than -28 dBc at 4.1 GHz.

From the measurements we can see, the proposed DPA can support concurrent operation with different frequency distribution and very large frequency spacing. It should be noticed that, there are a very few related reports under concurrent modulated signal stimulation with very large frequency spacing. In [37], [38], the designed dual-band PAs achieves 50% and 38% average drain efficiency in concurrent mode with frequency spacing of 700 MHz and less than 15 MHz signal bandwidth in each band. In [7], the frequency spacing in concurrent mode is increased to 1480 MHz while the average efficiency is 26.7%. Compared with these results and considering the frequency spacing, the proposed DPA presents comparable efficiency performance with good linearity and much more operation bands in concurrent mode.

C. Performance Comparison

The performance comparison with some recently published multi-band and broadband DPAs is summarized in Table VI. To the authors' knowledge, it is the first time that a 6-band DPA has been implemented. The proposed DPA shows comparable back-off efficiency performance with other multi-band or broadband DPAs and it can be used for multi-band applications with very large frequency spacing. From the measurement results we can see that, even only in Mode I, the spacing between the edge frequencies of the obtained two bands is more than one octave, while the back-off efficiency keeps higher than 49%. Compared with the proposed architecture, the reported broadband DPAs can barely achieve an octave bandwidth while obtaining comparable back-off efficiency performance in some specific frequency bands. Furthermore, by simply swapping gate biases, the proposed DPA can provide additional four operation bands which are distributed over a wider frequency range. Although the bandwidth of each band in Mode II is narrower than Mode I, at least 150 MHz bandwidth with high back-off efficiency is achieved, which is much wider than many other reported multi-band DPAs since they often only reported high back-off efficiency performance at each single operation frequency.

VI. CONCLUSION

This paper presents a novel method for designing multi-band DPAs. Phase periodic matching networks are used to realize impedance inverter and phase compensation function in wideband DPA structures. To validate the method, a dual-mode six-band DPA was designed and fabricated using commercial GaN devices. The measurement results showed that the operation bands of the proposed DPA distributed over a very wide frequency range covering multi octave bandwidth, that is usually very hard to achieve by normal broadband DPAs. In comparison with reported multi-band DPAs, the proposed DPA presents high back-off efficiency within hundred MHz bandwidth in each band while other works only reported comparable performance at single operation frequency. Despite dual-mode configuration slightly increases the system operation complexity, this configuration can be achieved by simply swapping the gate bias which is very easy to realize. The circuit complexity of the proposed DPA is comparable to other broadband or multi-band DPA solutions. In summary, the proposed DPA architecture provides a promising multi-band solution for broadband 5G wireless transmitters.

REFERENCES

[1] Huawei Technologies, "5G spectrum-Huawei," 2017. [Online]. Available: https://www-file.huawei.com/-/media/CORPORATE/PDF/public-policy/public_policy_position_5g_spectrum.pdf

[2] Qualcomm Technologies, "Spectrum for 4G and 5G," 2017. [Online]. Available: https://www.qualcomm.com/media/documents/files/spectrum-for-4g-and-5g.pdf

[3] L. Gupta, R. Jain, and G. Vaszkun, "Survey of important issues in UAV communication networks," *IEEE Commun. Surv. Tutor.*, vol. 18, no. 2, pp. 1123–1152, Secondquarter 2016.

[4] P. Saad, P. Colantonio, L. Piazzon, F. Giannini, K. Andersson, and C. Fager, "Design of a concurrent dual-band 1.8-2.4 GHz GaN-HEMT Doherty power amplifier," *IEEE Trans. Microw. Theory Techn.*, vol. 60, no. 6, pp. 1840–1849, Jun. 2012.

[5] W. Chen, S. A. Bassam, X. Li, Y. Liu, K. Rawat, M. Helaoui, F. M. Ghannouchi, and Z. Feng, "Design and linearization of concurrent dual-band Doherty power amplifier with frequency-dependent power ranges," *IEEE Trans. Microw. Theory Techn.*, vol. 59, no. 10, pp. 2537–2546, Oct. 2011.

[6] J. Pang, S. He, Z. Dai, C. Huang, J. Peng, and F. You, "Novel design of highly-efficient concurrent dual-band GaN Doherty power amplifier using direct-matching impedance transformers," in *2016 IEEE MTT-S International Microwave Symposium (IMS)*, May 2016, pp. 1–4.

[7] W. Chen, S. Zhang, Y. Liu, Y. Liu, and F. M. Ghannouchi, "A concurrent dual-band uneven Doherty power amplifier with frequency-dependent input power division," *IEEE Trans. Circuits Syst. Regul. Pap.*, vol. 61, no. 2, pp. 552–561, Feb. 2014.

[8] X. Li, M. Helaoui, F. Ghannouchi, and W. Chen, "A quad-band Doherty power amplifier based on T-section coupled lines," *IEEE Microw. Wirel. Compon. Lett.*, vol. 26, no. 6, pp. 437–439, Jun. 2016.

[9] R. Giofrè, L. Piazzon, P. Colantonio, and F. Giannini, "A closed-form design technique for ultra-wideband Doherty power amplifiers," *IEEE Trans. Microw. Theory Techn.*, vol. 62, no. 12, pp. 3414–3424, Dec. 2014.

[10] R. Kalyan, K. Rawat, and S. K. Koul, "Reconfigurable and concurrent dual-band Doherty power amplifier for multiband and multistandard applications," *IEEE Trans. Microw. Theory Techn.*, vol. 65, no. 1, pp. 198–208, Jan. 2017.

[11] A. M. M. Mohamed, S. Boumaiza, and R. R. Mansour, "Electronically tunable Doherty power amplifier for multi-mode multi-band base stations," *IEEE Trans. Circuits Syst. Regul. Pap.*, vol. 61, no. 4, pp. 1229–1240, Apr. 2014.

[12] X. A. Nghiem, J. Guan, T. Hone, and R. Negra, "Design of concurrent multiband Doherty power amplifiers for wireless applications," *IEEE Trans. Microw. Theory Techn.*, vol. 61, no. 12, pp. 4559–4568, Dec. 2013.

[13] X. Chen, W. Chen, F. M. Ghannouchi, Z. Feng, and Y. Liu, "A broadband Doherty power amplifier based on continuous-mode technology," *IEEE Trans. Microw. Theory Techn.*, vol. 64, no. 12, pp. 4505–4517, Dec. 2016.

[14] W. Shi, S. He, X. Zhu, B. Song, Z. Zhu, G. Naah, and M. Zhang, "Broadband continuous-mode Doherty power amplifiers with noninfinity peaking impedance," *IEEE Trans. Microw. Theory Techn.*, vol. 66, no. 2, pp. 1034–1046, Feb. 2018.

[15] C. Huang, S. He, and F. You, "Design of broadband modified class-J Doherty power amplifier with specific second harmonic terminations," *IEEE Access*, vol. 6, pp. 2531–2540, 2018.

[16] J. Pang, S. He, C. Huang, Z. Dai, J. Peng, and F. You, "A post-matching Doherty power amplifier employing low-order impedance inverters for Broadband Applications," *IEEE Trans. Microw. Theory Techn.*, vol. 63, no. 12, pp. 4061–4071, Dec. 2015.

[17] X. Y. Zhou, S. Y. Zheng, W. S. Chan, X. Fang, and D. Ho, "Postmatching Doherty power amplifier with extended back-off range based on self-generated harmonic injection," *IEEE Trans. Microw. Theory Techn.*, vol. 66, no. 4, pp. 1951–1963, Apr. 2018.

[18] J. Pang, S. He, Z. Dai, C. Huang, J. Peng, and F. You, "Design of a post-matching asymmetric Doherty power amplifier for broadband applications," *IEEE Microw. Wirel. Compon. Lett.*, vol. 26, no. 1, pp. 52–54, Jan. 2016.

[19] X. Y. Zhou, W. S. Chan, S. Y. Zheng, W. Feng, H. Liu, K. M. Cheng, and D. Ho, "A mixed topology for broadband high-efficiency Doherty power amplifier," *IEEE Trans. Microw. Theory Techn.*, vol. 67, no. 3, pp. 1050–1064, Mar. 2019.

[20] J. Xia, M. Yang, Y. Guo, and A. Zhu, "A broadband high-efficiency Doherty power amplifier with integrated compensating reactance," *IEEE Trans. Microw. Theory Techn.*, vol. 64, no. 7, pp. 2014–2024, Jul. 2016.

[21] J. Xia, W. Chen, F. Meng, C. Yu, and X. Zhu, "Improved three-stage Doherty amplifier design with impedance compensation in load combiner for broadband applications," *IEEE Trans. Microw. Theory Tech.*, vol. 67, no. 2, pp. 778–786, Feb. 2019.

[22] X. Fang, H. Liu, K. M. Cheng, and S. Boumaiza, "Modified Doherty amplifier with extended bandwidth and back-off power range using optimized peak combining current ratio," *IEEE Trans. Microw. Theory Techn.*, vol. 66, no. 12, pp. 5347–5357, Dec. 2018.

[23] X. H. Fang and K. M. Cheng, "Extension of high-efficiency range of Doherty amplifier by using complex combining load," *IEEE Trans. Microw. Theory Techn.*, vol. 62, no. 9, pp. 2038–2047, Sep. 2014.

[24] Z. Yang, Y. Yao, M. Li, Y. Jin, T. Li, Z. Dai, F. Tang, and Z. Li, "Bandwidth extension of Doherty power amplifier using complex combining load with noninfinity peaking impedance," *IEEE Trans. Microw. Theory Tech.*, vol. 67, no. 2, pp. 765–777, Feb. 2019.

[25] P. Saad, R. Hou, R. Hellberg, and B. Berglund, "A 1.8–3.8-GHz power amplifier With 40% efficiency at 8-dB power back-off," *IEEE Trans. Microw. Theory Techn.*, vol. 66, no. 11, pp. 4870–4882, Nov. 2018.

[26] P. H. Pednekar, E. Berry, and T. W. Barton, "RF-input load modulated balanced amplifier with octave bandwidth," *IEEE Trans. Microw. Theory Techn.*, vol. 65, no. 12, pp. 5181–5191, Dec. 2017.

[27] D. Y. Wu and S. Boumaiza, "A modified Doherty configuration for broadband amplification using symmetrical devices," *IEEE Trans. Microw. Theory Techn.*, vol. 60, no. 10, pp. 3201–3213, Oct. 2012.

[28] M. Li, J. Pang, Y. Li, and A. Zhu, "Ultra-wideband dual-mode Doherty power amplifier using reciprocal gate bias for 5G applications," *IEEE Trans. Microw. Theory Tech.*, vol. 67, no. 10, pp. 4246–4259, Oct. 2019.

[29] A. Cidronali, S. Maddio, N. Giovannelli, and G. Collodi, "Frequency analysis and multiline implementation of compensated impedance inverter for wideband Doherty high-power amplifier design," *IEEE Trans. Microw. Theory Techn.*, vol. 64, no. 5, pp. 1359–1372, May 2016.

[30] P. Colantonio, F. Giannini, R. Giofrè, and L. Piazzon, "The AB-C Doherty power amplifier. Part I: Theory," *Int. J. RF Microw. Comput.-Aided Eng.*, vol. 19, no. 3, pp. 293–306, Nov. 2008.

[31] ——, "The AB-C Doherty power amplifier. Part II: Validation," *Int. J. RF Microw. Comput.-Aided Eng.*, vol. 19, no. 3, pp. 307–316, Nov. 2008.

[32] K. Chen and D. Peroulis, "Design of highly efficient broadband class-E power amplifier using synthesized low-pass matching networks," *IEEE Trans. Microw. Theory Techn.*, vol. 59, no. 12, pp. 3162–3173, Dec. 2011.

[33] Z. Dai, S. He, F. You, J. Peng, P. Chen, and L. Dong, "A new distributed parameter broadband matching method for power amplifier via real frequency technique," *IEEE Trans. Microw. Theory Techn.*, vol. 63, no. 2, pp. 449–458, Feb. 2015.

[34] Z. Dai, S. He, J. Peng, C. Huang, W. Shi, and J. Pang, "A semianalytical matching approach for power amplifier with extended chebyshev function and real frequency technique," *IEEE Trans. Microw. Theory Techn.*, vol. 65, no. 10, pp. 3892–3902, Oct. 2017.

[35] J. Chani-Cahuana, P. N. Landin, C. Fager, and T. Eriksson, "Iterative learning control for RF power amplifier linearization," *IEEE Trans. Microw. Theory Techn.*, vol. 64, no. 9, pp. 2778–2789, Sep. 2016.

[36] R. Giofrè, L. Piazzon, P. Colantonio, and F. Giannini, "An ultra-broadband gan doherty amplifier with 83% of fractional bandwidth," *IEEE Microw. Wirel. Compon. Lett.*, vol. 24, no. 11, pp. 775–777, Nov. 2014.

[37] X. Chen, W. Chen, F. M. Ghannouchi, Z. Feng, and Y. Liu, "Enhanced analysis and design method of concurrent dual-band power amplifiers with intermodulation impedance tuning," *IEEE Trans. Microw. Theory Techn.*, vol. 61, no. 12, pp. 4544–4558, Dec. 2013.

[38] X. Chen, W. Chen, G. Su, F. M. Ghannouchi, and Z. Feng, "A concurrent dual-band 1.9–2.6-GHz Doherty power amplifier with intermodulation

impedance tuning," in *2014 IEEE MTT-S International Microwave Symposium (IMS2014)*, Jul. 2014, pp. 1–4.

Jingzhou Pang (S'13-M'16) received the B.S. degree in electrical engineering and Ph. D. degree in circuits and systems from University of Electronic Science and Technology of China (UESTC), Chengdu, China, in 2010 and 2016, respectively. In December 2016, he joined Huawei Technologies Company Ltd., Shenzhen, China, where he was a engineer in charge of the research and development of 5G high efficiency power amplifiers and transmitters. He is currently with the RF and Microwave Research Group at University College Dublin (UCD), Dubin, Ireland, as a research fellow. His research interests include broadband high-efficiency power amplifier systems, bandwidth extension techniques for high-efficiency transmitters and MMIC power amplifier design for RF/microwave and millimeter-wave applications.

Jingzhou Pang was a recipient of the EDGE Marie Sklodowska-Curie Individual Fellowship. He was a recipient of third Place Award of the High Efficiency Power Amplifier Student Design Competition, IEEE Microwave Theory and Techniques Society (IEEE MTT-S) International Microwave Symposium (IMS) in 2013.

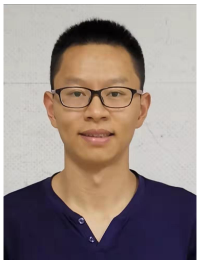

Zhijiang Dai (M'19) received the B.S. and Ph.D. degrees in electrical engineering from the University of Electronic Science and Technology of China, Chengdu, China, in 2011 and 2017, respectively. From 2017 to 2018, he was a research engineer with Huawei Technologies, where he focused on the study of MIMO wireless communication systems.

He is currently a Lecturer with the School of Microelectronics and Communication Engineering, Chongqing University, Chongqing, China. His research interests lie in the area of automatic matching techniques of PA, wideband and linear RF PA design, MIMO system.

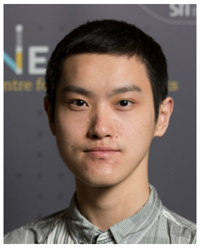

Yue Li (S'17) received the B.E. degree in information engineering from Southeast University, Nanjing, China, in 2016. He is currently working towards the Ph.D. degree at University College Dublin, Dublin, Ireland.

He is currently with the RF and Microwave Research Group, UCD. His current research interests include behavioral modeling and digital predistortion for RF power amplifiers.

Meng Li (S'14) received the B.S. degree in Electromagnetic Field and Radio Technology and M.S. degree in Electromagnetic Field and Microwave Technology from University of Electronic Science and Technology of China (UESTC), Chengdu, China, in 2012 and 2015, respectively, and is currently working towards the Ph.D degree at University College Dublin (UCD), Dublin, Ireland.

She is currently with the RF and Microwave Research Group, UCD. Her research interests mainly focus on broadband high-efficiency power amplifiers and MMIC power amplifier design for RF/microwave and millimeter-wave applications.

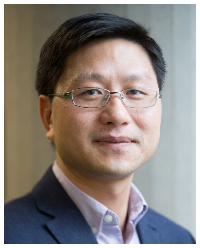

Anding Zhu (S'00-M'04-SM'12) received the Ph.D. degree in electronic engineering from University College Dublin (UCD), Dublin, Ireland, in 2004.

He is currently a Professor with the School of Electrical and Electronic Engineering, UCD. His research interests include high-frequency nonlinear system modeling and device characterization techniques, high-efficiency power amplifier design, wireless transmitter architectures, digital signal processing, and nonlinear system identification algorithms. He has published more than 130 peer-reviewed journal and conference articles.

Prof. Zhu is an elected member of MTT-S AdCom, the Chair of the Electronic Information Committee and the Vice Chair of the Publications Committee. He is also the Chair of the MTT-S Microwave High-Power Techniques Committee. He served as the Secretary of MTT-S AdCom in 2018. He was the General Chair of the 2018 IEEE MTT-S International Microwave Workshop Series on 5G Hardware and System Technologies (IMWS-5G) and a Guest Editor of the IEEE TRANSACTIONS ON MICROWAVE THEORY AND TECHNIQUES on 5G Hardware and System Technologies. He is currently an Associate Editor of the IEEE Microwave Magazine and a Track Editor of the IEEE TRANSACTIONS ON MICROWAVE THEORY AND TECHNIQUES.